JASA ARTICLE

# Toward optimal acoustophoretic microparticle manipulation by exploiting asymmetry[a)]

Amir Tahmasebipour,[1,b)] Leanne Friedrich,[2] Matthew Begley,[1,c)] Henrik Bruus,[3] and Carl Meinhart[1]
[1]*Department of Mechanical Engineering, University of California Santa Barbara, Santa Barbara, California 93106, USA*
[2]*Materials Department, University of California Santa Barbara, Santa Barbara, California 93106, USA*
[3]*Department of Physics, Technical University of Denmark, Danmarks Tekniske Universitet Physics Building 309, 2800 Kongens Lyngby, Denmark*

**ABSTRACT:**
The performance of a micro-acousto-fluidic device designed for microparticle trapping is simulated using a three-dimensional (3D) numerical model. It is demonstrated by numerical simulations that geometrically asymmetric architecture and actuation can increase the acoustic radiation forces in a liquid-filled cavity by almost 2 orders of magnitude when setting up a standing pressure half wave in a microfluidic chamber. Similarly, experiments with silicon-glass devices show a noticeable improvement in acoustophoresis of 20-$\mu$m silica beads in water when asymmetric devices are used. Microparticle acoustophoresis has an extensive array of applications in applied science fields ranging from life sciences to 3D printing. A more efficient and powerful particle manipulation system can boost the overall effectiveness of an acoustofluidic device. The numerical simulations are developed in the COMSOL Multiphysics® software package (COMSOL AB, Stockholm, Sweden). By monitoring the modes and magnitudes of simulated acoustophoretic fields in a relatively wide range of ultrasonic frequencies, a map of device performance is obtained. 3D resonant acoustophoretic fields are identified to quantify the improved performance of the chips with an asymmetric layout. Four different device designs are analyzed experimentally, and particle tracking experimental data qualitatively supports the numerical results. © *2020 Acoustical Society of America*.
https://doi.org/10.1121/10.0001634
(Received 29 March 2020; revised 25 June 2020; accepted 9 July 2020; published online 27 July 2020)
[Editor: Kedar Chitale] Pages: 359–373

## I. INTRODUCTION

Acoustophoresis offers active manipulation of microparticles in a fluid, independent of the flow field, and over the past decade, it has attracted a large array of applied fields from life sciences (Adams *et al.*, 2012; Petersson *et al.*, 2007) to three-dimensional (3D) printing (Collino *et al.*, 2016; Foresti *et al.*, 2018; Friedrich *et al.*, 2017) and material science (Begley *et al.*, 2019; Melchert *et al.*, 2019). The natural length scale of ultrasound waves in water, the millimeter-sized wavelength at low MHz frequencies, makes this method a prime candidate for microfluidic and lab-on-chip applications (Antfolk and Laurell, 2017; Augustsson *et al.*, 2009; Lin *et al.*, 2012; Ohlsson *et al.*, 2016). The high frequency nature of acoustophoretic force fields makes for robust yet gentle cell handling (Augustsson *et al.*, 2012; Burguillos *et al.*, 2013; Zalis *et al.*, 2016), which is ideal for biological applications like cell sorting (Thévoz *et al.*, 2010; Yang and Soh, 2012), cytometry (Grenvall *et al.*, 2012; Zmijan *et al.*, 2015), trapping (Evander *et al.*, 2007; Evander *et al.*, 2015; Hammarström *et al.*, 2010), and patterning (Collins *et al.*, 2015; Collins *et al.*, 2016; Shi *et al.*, 2009; Silva *et al.*, 2019). The precise manipulation of microparticles is made possible with the development of acoustic tweezers (Baresch *et al.*, 2016; Collins *et al.*, 2016) and complex transducer arrangements (Drinkwater, 2016).

The acoustic forces required for these applications rely on mechanical properties of the working fluid and particles (Antfolk *et al.*, 2014), as well as the ability to set up strong acoustofluidic fields in the device. Good acoustophoresis is possible through resonant actuation of the ultrasound waves while forming the desired mode for the purpose in mind (Hahn *et al.*, 2014). Most popular device designs are based on either bulk acoustic waves (BAWs; Reichert *et al.*, 2018) or surface acoustic waves (SAWs; Guo *et al.*, 2015; Skov *et al.*, 2019b), where BAW type devices have higher throughput. Efficient performance of the device is heavily impacted by design parameters, such as geometry (Garofalo *et al.*, 2017; Hahn *et al.*, 2014) and acoustic behavior of materials (Moiseyenko and Bruus, 2019).

Micro-acousto-fluidic devices can be fabricated from a variety of materials, depending on the preferred excitation method, intricacy of geometry, required force fields, sensitivity to heat, and budget. BAW type devices can be made from affordable materials, such as aluminum (Gautam *et al.*, 2018), glass capillary tubes (Hammarström *et al.*, 2012; Hammarström *et al.*, 2014), or easily fabricated polymers

[a)]This paper is part of the special issue on Theory and applications of Acoustofluidics.
[b)]Electronic mail: atahmasebipour@ucsb.edu, ORCID:0000-0002-5861-174X.
[c)]Also at: Materials Department, University of California Santa Barbara, Santa Barbara, CA 93106, USA.

(González *et al.*, 2015; Lissandrello *et al.*, 2018). On the other hand, highly efficient bonded silicon-glass chips offer higher resonance amplitudes because of lower acoustic losses and a high acoustic impedance compared to water with the drawback of being more expensive and challenging to fabricate due to the required bonding process (Samarasekera and Yeow, 2015).

There are numerous successful attempts at using acoustophoresis for particle handling and many experimental techniques that achieve satisfactory results, yet, the design and development process of acoustofluidic devices can be improved. Backed by a strong theoretical framework, our understanding of this phenomenon can grow to utilize the complex interplay between various physics at play to make more effective, well characterized, and overall better devices (Iranmanesh *et al.*, 2013; Karthick and Sen, 2018).

In this work, numerical simulation tools are used to calculate damped 3D acoustic fields in a BAW type silicon-glass device designed for particle manipulation. We process these results to characterize the frequency response of the device and identify good acoustophoresis based on established criteria. We then apply this method to analyze the effects of breaking geometric symmetry (Laurell and Lenshof, 2014) on acoustophoretic behavior of our system. Finally, to compare particle manipulation in different devices as a function of geometric asymmetry, we perform a series of experiments and analyze particle aggregation properties through image processing techniques.

## II. ACOUSTOFLUIDIC DEVICE SIMULATION

### A. Device geometry and materials

A typical BAW acoustofluidic device is made up of a microfluidic chip on top of a piezo transducer. The general layout of devices used in this paper for numerical and experimental studies of acoustophoresis is presented in Fig. 1. The microchannel consists of a square chamber, where the goal here is to collect particles as shown in Fig. 1(a).

Devices with similar geometries have been used in previous experimental (Hagsäter *et al.*, 2007; Manneberg *et al.*, 2008; Ohlin *et al.*, 2015) and theoretical studies (Hahn *et al.*, 2014; Hahn and Dual, 2015; Skov *et al.*, 2019a). The rectangular fluid channel extends along the $x$ axis, and the entire cavity has a uniform height. Figure 1(b) presents a $y$-$z$ cross section of the device passing through the origin of the right-handed coordinate system, which we assume to be placed at the center of the chamber for the remainder of this paper. We introduce parameters $l_s$ and $\alpha$ to define asymmetry of the device based on the shifted transducer placement and asymmetric chip design as sketched in Figs. 1(a) and 1(b). The chip is considered to be symmetric only when the asymmetry factor $\alpha = 1$ as this means that the channel side walls are equally distanced from the outer walls. We also express symmetric placement of the piezo when the transducer shift $l_s = 0$ mm. Table I lists all geometric parameters and their values. Additionally, asymmetry can be introduced by driving the left and right sides of the piezo in antiphase.

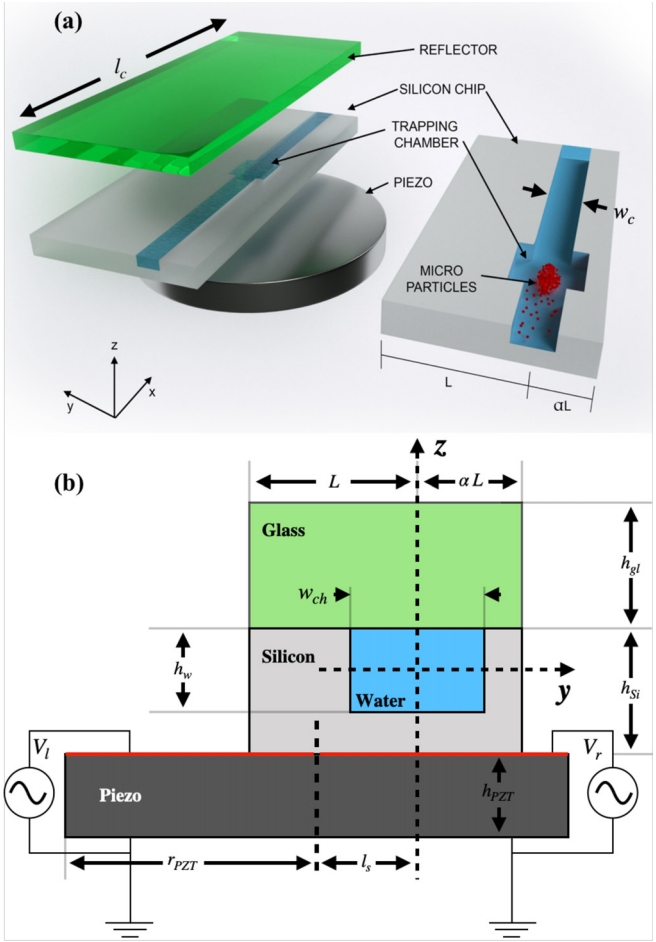


FIG. 1. (Color online) (a) Sketch of the acoustofluidic device with an exploded view of all components and a qualitative illustration of the microparticle manipulation. (b) Cross section of the device, taken at the center of the chamber, to clearly show geometrical parameters. The electrode configuration facilitates actuation of the left and right sides of the piezo transducer in phase or antiphase.

This can be realized by using a split top electrode as studied in Moiseyenko and Bruus (2019) to allow for antisymmetric excitation of the devices.

The microfluidic chip is made of silicon for its low acoustic attenuation (Evander *et al.*, 2008; Nama *et al.*, 2015) and high specific impedance as compared to water (Leibacher *et al.*, 2014b; Lenshof *et al.*, 2012) and is suitable for creating hard walls (Leibacher *et al.*, 2015; Muller *et al.*, 2012) around the water-filled cavity. A glass (Pyrex) reflector layer (Augustsson *et al.*, 2011; Barnkob *et al.*, 2012; Muller *et al.*, 2013) is employed to facilitate imaging of the acoustophoresis inside the chamber. The transducer material, lead zirconate titanate (PZT), is a low permittivity and fine-grained piezoelectric ceramic, which is ideal for high frequency resonance applications, offering a high mechanical quality factor and low dielectric loss (Ferroperm, Meggitt A/S, Kvistgaard, Denmark).

### B. Governing equations

The 3D model of the acoustofluidic device consists of an elastic solid chip that is actuated by a piezoelectric

https://doi.org/10.1121/10.0001634

TABLE I. Geometry parameters for solid and fluid domains of the device studied in this paper.

| Parameter | Symbol | Value |
|---|---|---|
| Channel length | $l_c$ | 20 mm |
| Channel width | $w_c$ | 350 $\mu$m |
| Channel height | $h_w$ | 150 $\mu$m |
| Glass height | $h_{\mathrm{gl}}$ | 500 $\mu$m |
| Silicon height | $h_{\mathrm{Si}}$ | 525 $\mu$m |
| Piezo height | $h_{\mathrm{PZT}}$ | 1 mm |
| Piezo radius | $r_{\mathrm{PZT}}$ | 5 mm |
| Chip size | $L$ | 4 mm |
| Chamber width | $w_{\mathrm{ch}}$ | 800 $\mu$m |

material while fluid-structure interactions at the walls of the embedded channel produce acoustic fields within the fluid-filled cavity. Therefore, linear elastodynamics equations need to be solved in all solid domains (Dual and Schwarz, 2012) and coupled with Gauss's law through constitutive relations applied to the piezo domain (Dual and Möller, 2012).

The physics of the fluid is governed by the continuity and Navier-Stokes equations (Bruus, 2011). In this work, transient response (Muller and Bruus, 2015) and thermoviscous effects (Karlsen and Bruus, 2015; Muller and Bruus, 2014) are disregarded so only isentropic, time harmonic fields need to be resolved at ambient temperatures. We formulate the relevant equations in the frequency domain by using the Fourier representation of time domains $A(\mathbf{r}, t) = A(\mathbf{r}, \omega)\, e^{-i\omega t}$, where $\mathbf{r}$ and $t$ denote space and time and $\omega = 2\pi f$ is the angular frequency corresponding to the actuation frequency $f$. The real part of this field, $\mathrm{Re}[A(\mathbf{r}, \omega)\, e^{-i\omega t}]$, corresponds to the physical values.

To model the dynamics of the homogeneous solids, we solve the Cauchy equation of motion in the frequency domain,

$$\rho_{\mathrm{sl}}\omega^2\mathbf{u} + \nabla\cdot\boldsymbol{\sigma}_{\mathbf{s}} = 0, \tag{1}$$

where $\rho_{\mathrm{sl}}$ is the density, $\mathbf{u}$ is the displacement field, and $\boldsymbol{\sigma}_{\mathbf{s}}$ represents the stress tensor in the solid. Stress and displacement are related by Hooke's law, expressed in terms of elasticity and strain,

$$\boldsymbol{\sigma}_{\mathbf{s}} = \mathbf{C} : \boldsymbol{\epsilon}, \tag{2}$$

where $\mathbf{C}$ is the stiffness or elasticity tensor, and the strain tensor $\boldsymbol{\epsilon} = \frac{1}{2}\left[\nabla\mathbf{u} + (\nabla\mathbf{u})^T\right]$ is derived from the displacement field.

In order to solve for the displacement field of piezoelectric solids, the equation of motion should be coupled with Gauss's law because the stress and electric charge are mutually dependent. The coupled constitutive equations, in addition to Eq. (1), are given by

$$\nabla\cdot\mathbf{D} = 0, \tag{3a}$$

$$\boldsymbol{\sigma}_{\mathbf{s}} = \mathbf{C} : \boldsymbol{\epsilon} + \boldsymbol{d}^T\cdot\nabla V, \tag{3b}$$

$$\mathbf{D} = \boldsymbol{d} : \boldsymbol{\epsilon} - \varepsilon_o\boldsymbol{\varepsilon}_{\mathbf{rs}}\cdot\nabla V, \tag{3c}$$

where $\mathbf{D}$ is the electric displacement field, $V$ is the electrostatic potential, and $\boldsymbol{d}$ is the piezo coupling tensor. Relative permittivity of free space is denoted by $\varepsilon_o$, whereas $\boldsymbol{\varepsilon}_{\mathbf{rs}}$ is the relative permittivity tensor under constant strain.

In the cavity filled with a fluid of density $\rho_{\mathrm{fl}}$ and speed of sound $c_{\mathrm{fl}}$, the governing equations can be simplified by applying the perturbation theory (Bach and Bruus, 2018; Bruus, 2012a) to find the first-order time harmonic acoustic pressure $p$ and velocity $\mathbf{v}$ fields for an inviscid fluid in the frequency domain,

$$\nabla^2 p + \frac{\omega^2}{c_{\mathrm{fl}}}p = 0, \tag{4a}$$

$$\mathbf{v} = -\frac{i}{\omega\,\rho_{\mathrm{fl}}}\nabla p. \tag{4b}$$

### C. Material properties and attenuation factors

In solid domains, the elastic behavior is defined by the stiffness tensor shown in Voigt notation,

$$\mathbf{C} = \begin{bmatrix} C_{11} & C_{12} & C_{12} & 0 & 0 & 0 \\ C_{12} & C_{11} & C_{12} & 0 & 0 & 0 \\ C_{12} & C_{12} & C_{11} & 0 & 0 & 0 \\ 0 & 0 & 0 & C_{44} & 0 & 0 \\ 0 & 0 & 0 & 0 & C_{44} & 0 \\ 0 & 0 & 0 & 0 & 0 & C_{44} \end{bmatrix}, \tag{5}$$

where for an isotropic solid like Pyrex, the elastic moduli are not independent such that $C_{44} = (C_{11} - C_{12})/2$, and the stiffness matrix can be expressed in terms of Young's modulus $E$ and Poisson's ratio $\nu$ as

$$C_{11} = \frac{E\,(1-\nu)}{(1+\nu)\,(1-2\nu)}, \tag{6a}$$

$$C_{12} = \frac{E\,\nu}{(1+\nu)\,(1-2\nu)}. \tag{6b}$$

For the piezoelectric material, the coupling and permittivity matrices are given in addition to the nonsymmetric stiffness tensor,

$$\mathbf{C}_{\mathrm{pzt}} = \begin{bmatrix} C_{11} & C_{22} & C_{13} & 0 & 0 & 0 \\ C_{21} & C_{22} & C_{23} & 0 & 0 & 0 \\ C_{31} & C_{32} & C_{33} & 0 & 0 & 0 \\ 0 & 0 & 0 & C_{44} & 0 & 0 \\ 0 & 0 & 0 & 0 & C_{55} & 0 \\ 0 & 0 & 0 & 0 & 0 & C_{66} \end{bmatrix}, \tag{7a}$$

$$\boldsymbol{d}_{\mathrm{pzt}} = \begin{bmatrix} 0 & 0 & 0 & 0 & d_{15} & 0 \\ 0 & 0 & 0 & d_{15} & 0 & 0 \\ d_{31} & d_{31} & d_{33} & 0 & 0 & 0 \end{bmatrix}, \tag{7b}$$

$$\boldsymbol{\varepsilon}_{\mathrm{pzt}} = \begin{bmatrix} \varepsilon_{11} & 0 & 0 \\ 0 & \varepsilon_{11} & 0 \\ 0 & 0 & \varepsilon_{33} \end{bmatrix}, \tag{7c}$$

completing the required material properties to solve Eqs. (1)–(3c) for obtaining the displacement and potential fields.

The damping of acoustic waves in the lossy linear elastic materials is taken into account by splitting the fourth-order stiffness tensor $\mathbf{C}$ into storage and loss tensors $\mathbf{C}'$ and $\mathbf{C}''$, respectively (Hahn and Dual, 2015), as

$$\mathbf{C} = \mathbf{C}' + i\mathbf{C}''. \tag{8}$$

Material properties required for constructing these tensors for linear solids, as well as damping factors for the piezo, are listed in Table II.

In the fluid, one needs to know density and speed of sound to solve the governing equations. To calculate attenuation factors and efficiently dampen the acoustic resonances in our model, we use a two-step method described extensively in Hahn and Dual (2015) as the acoustic modes play an important role in determining loss coefficients. We apply the total acoustofluidic loss factor as

$$c_{\mathrm{fl}} = c_0 \left(1 + i\frac{\varphi_{\mathrm{fl}}}{2}\right), \tag{9}$$

where the frequency-dependent total acoustofluidic loss factor $\varphi_{\mathrm{fl}}(f) \ll 1$ is assumed to be due to the viscosity in the bulk of the fluid in addition to the viscous boundary layer at the cavity walls. We only include these two loss mechanisms because they contribute a leading majority to the total loss factor in the fluid (Hahn and Dual, 2015). As the first step, we choose the estimated loss factor in the viscous boundary layer $\tilde{\varphi}_{\mathrm{fl}}(f) = \delta S_{\mathrm{fl}}/2V_{\mathrm{fl}}$, where $S_{\mathrm{fl}}$ and $V_{\mathrm{fl}}$ denote wetted area and fluid volume, respectively, while the boundary layer thickness $\delta = \sqrt{2\eta_{\mathrm{fl}}/\rho_{\mathrm{fl}}\omega}$ changes with actuation frequency. Values for the viscous loss factors in the bulk, $\varphi_\eta$, and the boundary layer, $\varphi_\delta$, for a fluid with dynamic viscosity, $\eta_{\mathrm{fl},d}$, and bulk viscosity, $\eta_{\mathrm{fl},b}$, are calculated in the first step as

$$\varphi_\eta = \frac{\omega}{\rho_{\mathrm{fl}}\, c_0^2}\left(\frac{4}{3}\,\eta_{\mathrm{fl},d} + \eta_{\mathrm{fl},b}\right), \tag{10a}$$

$$\varphi_\delta = \frac{\rho_{\mathrm{fl}}\,\delta}{4\,E_{\mathrm{st}}^{\mathrm{fl}}}\int_{S_{\mathrm{fl}}} \sum (\xi_i)(\xi_i)^* \mathrm{d}S_{\mathrm{fl}}, \tag{10b}$$

where $E_{\mathrm{st}}^{\mathrm{fl}} = \int_{V_{\mathrm{fl}}} (2\,\rho_{\mathrm{fl}}\, c_0^2)^{-1}\,\langle p^2\rangle \mathrm{d}V_{\mathrm{fl}}$ is the stored energy in the fluid and $\xi_i = v_i - \dot{u}_i$ is the relative velocity of the fluid and solid domains at the walls. The total fluid domain damping factor used in the second step then becomes $\varphi_{\mathrm{fl}} = \varphi_\eta + \varphi_\delta$.

### D. Boundary conditions

In the following, we summarize the boundary conditions applied across material domains that are mentioned

TABLE II. List of material properties and damping factors at 25 °C and frequency of 1 MHz.

| Parameter | Symbol and value | Unit |
|---|---|---|
| Water parameters (Hahn *et al.*, 2014; Muller and Bruus, 2014) | | |
| Speed of sound | $c_{\mathrm{fl}} = 1500$ | $\mathrm{m\,s^{-1}}$ |
| Density | $\varrho_{\mathrm{fl}} = 998$ | $\mathrm{kg\,m^{-3}}$ |
| Dynamic viscosity | $\eta_{\mathrm{fl},d} = 0.89$ | mPa s |
| Bulk viscosity | $\eta_{\mathrm{fl},b} = 2.485$ | mPa s |
| Estimate loss factor | $\tilde{\varphi}_{\mathrm{fl}} = 0.005$ | |
| Pyrex parameters (\| Schott North America, glass manufacturers and processing, Elmsford, NY; Hahn and Dual, 2015) | | |
| Density | $\varrho_{\mathrm{py}} = 2240$ | $\mathrm{kg\,m^{-3}}$ |
| Young's modulus | $E_{\mathrm{py}} = (1 + i\,0.0004)\,60$ | GPa |
| Poisson's ratio | $\nu_{\mathrm{py}} = 0.245$ | |
| Silicon parameters (Hopcroft *et al.*, 2010) | | |
| Density | $\varrho_{\mathrm{si}} = 2330$ | $\mathrm{kg\,m^{-3}}$ |
| Stiffness matrix | $\mathbf{C}_{\mathrm{si}} = (1 + i\,0)\,C_{\mathrm{nn}}$, with | |
| | $C_{11} = 166,\ C_{12} = 64,\ C_{44} = 80$ | GPa |
| Pz26 parameters (Garofalo *et al.*, 2017; Hahn *et al.*, 2014; Ferroperm, Meggitt A/S, Kvistgaard, Denmark) | | |
| Density | $\varrho_{\mathrm{pzt}} = 7700$ | $\mathrm{kg\,m^{-3}}$ |
| Stiffness matrix | $\mathbf{C}_{\mathrm{pzt}} = (1 + i\,0.01)\,C_{\mathrm{nn}}$, with | |
| | $C_{11} = C_{22} = 168$ | GPa |
| | $C_{12} = 110,\ C_{13} = C_{23} = 99.9$ | GPa |
| | $C_{33} = 123,\ C_{44} = C_{55} = 30.1$ | GPa |
| | $C_{66} = 29$ | GPa |
| Permittivity tensor | $\varepsilon_{\mathrm{pzt}} = (1 - i\,0.003)\,\varepsilon_{\mathrm{nn}}$, with | |
| | $\varepsilon_{11} = \varepsilon_{22} = 828,\ \varepsilon_{33} = 700$ | |
| Coupling matrix | $d_{\mathrm{pzt}} = (1 + i\,0.035)\,d_{\mathrm{nn}}$, with | |
| | $d_{15} = 9.86,\ d_{31} = -2.8$ | $\mathrm{C\,m^{-2}}$ |
| | $d_{33} = 14.7$ | $\mathrm{C\,m^{-2}}$ |

https://doi.org/10.1121/10.0001634

above. The outer boundaries of the solid domains are free to vibrate, and the stresses and displacements are continuous in solid–solid interfaces,

$$\text{solid–air} \quad \boldsymbol{\sigma}_{\mathbf{s}} \cdot \hat{\boldsymbol{n}} = 0, \tag{11a}$$

$$\text{solid–solid} \quad \mathbf{u}_{\mathrm{s}1} = \mathbf{u}_{\mathrm{s}2} \text{ and } (\boldsymbol{\sigma}_{\mathrm{s}1} - \boldsymbol{\sigma}_{\mathrm{s}2}) \cdot \hat{\boldsymbol{n}} = 0. \tag{11b}$$

The applied electrostatic potential to the piezo transducer boundaries is such that the piezo is grounded at the bottom and a potential of $V_p$ is applied to the top electrodes. We assume zero charge on the sides,

$$\text{piezo bottom} \quad V = 0, \tag{12a}$$

$$\text{piezo top (in phase)} \quad V_l = V_r = V_p, \tag{12b}$$

$$\text{piezo top (anti phase)} \quad V_l = -V_r = V_p, \tag{12c}$$

$$\text{piezo side} \quad \mathbf{D} \cdot \hat{\boldsymbol{n}} = 0, \tag{12d}$$

where Eq. (12b) is applied to the entire top surface of the transducer for in phase actuation (see animation SuppPubmm1.mp4 in the supplementary material).[1] Equation (12c) applies to the antisymmetric excitation scenario when the left and right sides of the piezo are actuated in antiphase (see animation SuppPubmm2.mp4 in the supplementary material).[1]

The next set of boundary conditions defines the acoustic fluid–structure interactions that produce the scattered acoustofluidic fields inside the cavity. This fluid–solid coupling at the boundary can be modeled by imposing the same acceleration at the fluid–solid interface and applying the pressure in the fluid as a boundary load to the solid domain,

$$\text{normal stress} \quad \boldsymbol{\sigma}_{\mathbf{s}} \cdot \hat{\boldsymbol{n}} = -p, \tag{13a}$$

$$\text{acceleration} \quad \frac{\boldsymbol{\nabla} p}{\rho_{\mathrm{fl}}} \cdot \hat{\boldsymbol{n}} = -\omega^2 \, \mathbf{u} \cdot \hat{\boldsymbol{n}}, \tag{13b}$$

and at the inlet and outlet, a zero pressure condition is dictated,

$$\text{air–fluid} \quad p = 0. \tag{13c}$$

### E. Time-averaged fields and acoustophoresis of microparticles

In this work, we aim to characterize the performance of acoustofluidic devices and properly find resonance frequencies resulting in strong acoustic fields. The average energy density is a good measure of these resonant fields. In the solid domain, the combined elastic and kinetic energy densities are used to find

$$E_{\mathrm{ac}}^{\mathrm{sl}} = \frac{1}{2} \left( \rho_{\mathrm{sl}} \omega^2 \langle u_i u_i \rangle + \langle \epsilon_{ij} \sigma_{ij} \rangle \right), \tag{14a}$$

where $\langle AB \rangle = \frac{1}{2} \mathrm{Re}(A^* B)$ is the time average of the time harmonic fields $A$ and $B$ over one period, and parameters are summed over the repeated indices $i,j = x,y,z$. By taking the average of the energy density over the solid domains, we calculate $\bar{E}_{\mathrm{ac}}^{\mathrm{sl}}$, the volume-averaged energy density. Similarly, in the fluid domain, the volume average of the energy density $\bar{E}_{\mathrm{ac}}^{\mathrm{fl}}$ is calculated from

$$E_{\mathrm{ac}}^{\mathrm{fl}} = \frac{1}{2} \left( \rho_{\mathrm{fl}} \langle v_i v_i \rangle + \kappa_{\mathrm{fl}} \langle p^2 \rangle \right), \tag{14b}$$

where $\kappa_{\mathrm{fl}} = (\rho_{\mathrm{fl}} \, c_{\mathrm{fl}}^2)^{-1}$ is the compressibility of the fluid.

Acoustic fields with a wavelength $\lambda$ apply forces on a particle with radius $a \ll \lambda$, which can be classified into three groups: the acoustic radiation force, the secondary acoustic radiation force, and the streaming induced drag force. In this paper, we use 20-$\mu$m silica microbeads with material properties similar to those of Pyrex. For these particles, the radiation force becomes the dominant mode of acoustophoresis as the radius is well above the critical value of $a_c \approx 0.75$ $\mu$m (Bruus, 2012b; Muller *et al.*, 2012); therefore, we do not expect significant interference from acoustic streaming rolls. On the other hand, the secondary radiation or Bjerknes force (Bjerknes, 1906; Doinikov, 1999; Doinikov and Zavtrak, 1995) that arises from the interaction between particles can become significant compared to the acoustic radiation force when particles are close to one another (Lopes *et al.*, 2016; Silva and Bruus, 2014) or the radiation force is locally small. The acoustic radiation force is given by the negative gradient of the radiation potential (Gor'kov, 1962; Settnes and Bruus, 2012),

$$\mathbf{F}^{\mathrm{rad}} = -\boldsymbol{\nabla} U^{\mathrm{rad}}, \tag{15a}$$

$$U^{\mathrm{rad}} = \frac{4}{3} \pi a^3 \left[ f_1 \frac{\kappa_{\mathrm{fl}}}{2} \langle p^2 \rangle - f_2 \frac{3 \rho_{\mathrm{fl}}}{4} \langle v_i v \rangle_i \right], \tag{15b}$$

where $f_1 = 1 - (\kappa_p / \kappa_{\mathrm{fl}}) = 0.94$ is the monopole and $f_2 = (2\rho_p - 2\rho_{\mathrm{fl}})/(2\rho_p + \rho_{\mathrm{fl}}) = 0.45$ is the dipole acoustic scattering coefficient for silica particles with radius $a$ suspended in water. The Stokes' drag (Bruus, 2011) on the particle is given by

$$\mathbf{F}^{\mathrm{drag}} = 6\pi a \eta_{\mathrm{fl}} (\mathbf{v}_{\mathrm{fl}} - \mathbf{v}_p), \tag{16}$$

and the secondary radiation force $\boldsymbol{F}^B$ from the particle interactions can be formulated (Silva and Bruus, 2014) as

$$\mathbf{F}^B = 4\pi a^6 \left[ \frac{(\rho_p - \rho_{\mathrm{fl}})^2 (3 \cos^2\theta - 1)}{6 \rho_{\mathrm{fl}} d^4} \left( \frac{\boldsymbol{\nabla} p}{\rho_{\mathrm{fl}} \omega} \right)^2 - \frac{\omega^2 \rho_{\mathrm{fl}} (\kappa_p - \kappa_{\mathrm{fl}})^2}{9 d^2} p^2 \right], \tag{17}$$

where $d$ is the distance between two particles and $\theta$ is the angle between the line connecting the particles and the axis of the standing wave.

Equations (15)–(17) summarize forces that particles experience while inside a micro-acousto-fluidic device. Particle manipulation inside the cavity is a result of these

force fields. Therefore, device performance can be defined by calculating the dominant force field inside the chamber.

### F. Numerical implementation

We implement the governing equations (1)–(4b) subject to boundary conditions shown by Eqs. (11a)–(13) in the finite element solver COMSOL Multiphysics® 5.4a (COMSOL AB, Stockholm, Sweden). We solve for pressure, displacement, and electric potential field in relevant domains on a grid made up of second-order elements with more than $10^6$ degrees of freedom. We perform a grid convergence study with a procedure similar to that of Ley and Bruus (2017), results of which are included in the supplementary material (see SuppPub1.pdf, Sec. A).[1]

We sweep the actuation frequency, as well as the geometrical parameters, to obtain the frequency responses for six distinctive devices listed in Table III [a more descriptive version of Table III is included in the supplementary material (see Table I of SuppPub1.pdf)].[1] We use Eqs. (14) and (15) in order to characterize the devices and measure the quality of acoustophoresis.

## III. EXPERIMENTAL SETUP, PROCEDURE AND ANALYSIS

### A. Chip and experimental setup

Glass-on-silicon microfluidic chips were fabricated as described in Collino *et al.* (2015). Inlets were attached to the silicon side of the chip to enable viewing on an inverted light microscope. A piezoelectric actuator (10 mm × 1 mm thick PZT-Navy I material, American Piezo, Mackeyville, PA) was coupled to the device using a thin layer of ultrasonic gel and held in place with an insulated paperclip. The chip and piezo assembly were gently fastened to the stage and placed on soft tissues to minimize anchor losses (Hahn and Dual, 2015). To ensure consistency and accuracy of piezo placement, the distance between the lateral edges of the chip and transducer were monitored throughout the experiment by analyzing the microscope images. During the device testing period, no signs of overheating or evaporation of the liquid gel were observed. The piezo was driven using an amplifier (Mini-Circuits LZY-22+, Brooklyn, NY) connected to a signal generator (HP 33120 A, Palo Alto, CA). Sinusoidal signals were generated at a peak-to-peak voltage of 40 $V_{pp}$.

Silica microspheres (Corpuscular C-SIO-20.0, Cold Spring, NY) with a 20 $\mu$m diameter were diluted to 5 wt% in deionized water and driven through the devices manually using a syringe. Videos were collected under non-flowing conditions using an inverted light microscope (Nikon TI-U Eclipse, Melville, NY) and a PointGrey Grasshopper camera (GS3-U3-2356C-C, Wilsonville, OR).

TABLE III. List of geometry parameters for simulated acoustofluidic devices. Nondimensional chip asymmetry factor $\alpha$ and shifted piezo placement $l_s$ are chosen such that the distance travelled by the acoustic wave to the solid-air, sound hard boundaries is altered by $\lambda\left(1+\frac{1}{4}\right)$ in each case.

| Device | $\alpha$ | $l_s$ |
|---|---|---|
| D1 | 1 | 0 mm |
| D2 | 1 | 2 mm |
| D3 | 0.5 | 2 mm |
| D4 | 0.5 | 0 mm |
| D1a | 1 | 0 mm |
| D4a | 0.5 | 0 mm |

### B. Experimental procedure

The experiments are designed to capture the acoustophoretic motion of the particles under a standing half wave pressure field in the fluidic chamber. To set up a half wave resonance with $\lambda = 2w_{ch}$, the frequency is tuned around the theoretically expected resonant frequency (Barnkob *et al.*, 2010),

$$f_0 = \frac{c_{fl}}{2w_{ch}} = 0.9375 \text{ MHz}, \tag{18}$$

and after finding a strong resonance, the particles are focused at a distance $w_{ch}/4$ from the center of the chamber by tuning the frequency to $f = 2f_0$. Afterward, we switch to the previously identified half wave resonance frequency and capture the transverse and axial paths of the particles.

### C. Analysis of experimental data

Neglecting the inertial effects and axial particle migration, we can use a theoretical relation for the particle path as a function of time given by Barnkob *et al.* (2010). By balancing the acoustic radiation force [Eq. (15)] and Stokes' drag [Eq. (16)], the expression for the transverse position $y$ with respect to time $t$ is obtained as

$$y(t) = \frac{\pi}{w_{ch}} \tan^{-1}\left\{\tan\left[\frac{w_{ch}}{\pi} y(0)\right] \exp\left[\frac{4\Phi}{3\eta_{fl}}\left(\frac{w_{ch}}{\pi} a\right)^2 E_{ac} t\right]\right\}, \tag{19a}$$

$$\Phi = \frac{\rho_p + \frac{2}{3}(\rho_p - \rho_{fl})}{2\rho_p + \rho_{fl}} - \frac{1}{3}\frac{\rho_{fl}\, c_{fl}^2}{\rho_p\, c_p^2}, \tag{19b}$$

where $\Phi$ is the acoustic contrast factor (Augustsson *et al.*, 2010). This function should accurately fit the particle paths in locations where the radiation force $\boldsymbol{F}^{rad}$ is considerably larger than the streaming drag and secondary radiation force $\boldsymbol{F}^{B}$. Knowing that in a standing half wave acoustic field, the radiation force decreases as particles migrate toward the center and inter-particle interaction forces increase as the particles aggregate, we can write a scaling relationship (Collino *et al.*, 2018) for these acoustophoretic effects as the particles approach the middle of the chamber,

$$\frac{\boldsymbol{F}^{B}}{\boldsymbol{F}^{rad}} = \tilde{a}^3\left[\frac{\tilde{\alpha}_\rho}{\tilde{d}^4}(3\cos^2\theta - 1)\cos^2\pi\tilde{y} - \frac{\tilde{\alpha}_\kappa}{\tilde{d}^2}\sin^2\pi\tilde{y}\right], \tag{20}$$

https://doi.org/10.1121/10.0001634

where $\tilde{a}$, $\tilde{d}$, and $\tilde{y}$ are the nondimensional particle radius, inter-particle distance, and location, respectively, with respect to the chamber width. Pre-factors $\tilde{\alpha}_\rho = (1/3\pi\Phi)(\rho_p/\rho_{\mathrm{fl}} - 1)^2$ and $\tilde{\alpha}_\kappa = (8\pi/9\Phi)(\kappa_p/\kappa_{\mathrm{fl}} - 1)^2$ are used for brevity. For our experiments, using Eq. (20) while assuming a symmetric transverse approach of particles where $\theta = 0$ and $\tilde{d} = 2\tilde{y}$, the repulsive $\boldsymbol{F}^B$ exceeds 15% of the attractive $\boldsymbol{F}^{\mathrm{rad}}$ when particles have cleared 80% of their transverse path. Therefore, due to close packing, the interference from the Bjerknes forces becomes considerable and Eq. (19a) cannot represent paths of particles beyond this point in space.

## IV. RESULTS

The main goal of the device we study in this work is to create an acoustophoretic force field inside the microfluidic chamber to trap microbeads as shown in Fig. 1. In order to establish criteria for good trapping acoustophoresis, we begin by analyzing the characteristics of a device that successfully fulfills this goal. Subsequently, we compare the results obtained from 3D models of six devices with different designs and actuation methods to show the effects of breaking symmetry on the quality of microparticle trapping. Finally, we present experimental results to demonstrate effective acoustic manipulation of silica microspheres.

### A. Device characterization

We use the numerical simulation method explained in Sec. II to solve for time harmonic acoustic fields in the piezo transducer, silicon-glass chip, and the water-filled cavity. Using the displacement field **u** in solid parts, as well as the first-order pressure field $p_1$ in the fluid domain, we aim to characterize the device's performance and especially look for circumstances where the acoustic radiation force field in the micro-chamber is suitable for trapping the particles. Such results are illustrated in Fig. 2 where we consider device D4, a chip with asymmetry factor $\alpha = 0.5$ and transducer shift $l_s = 0$ mm, as an example.

As expected, at frequencies around $f_0$, a resonant standing pressure half wave [Fig. 2(b)] forms across the chamber, indicating a strong force field, which is very desirable for effective particle manipulation. It is observed that this pressure distribution is accompanied by an antisymmetric translation of the side walls of the chamber while a ripple forms on the top and bottom walls of our micro-cavity [Fig. 2(e)]. The combination of these two displacement patterns resembles a bulge and pinch deforming the surroundings of the trapping area harmonically [Fig. 2(b); see animation SuppPubmm3.mp4 in the supplementary material].[1]

As discussed earlier in Sec. II, the modes and magnitudes of pressure, velocity, and displacement fields play an important role in determining damping factors and acoustic radiation force fields at any frequency. However, since our objective is to study trapping force fields, it is more fruitful to focus on the acoustic radiation force potential $U^{\mathrm{rad}}$ in the interest of simplicity and efficiency of our device characterization. This potential field can be practically represented by a slice in the $x$-$y$ plane since its variations in the $z$-direction are negligible in the bulk part of the fluid [Fig. 2(a)].

Figure 2(c) shows that the virtually perfect standing pressure half wave in the $y$-direction produces a $U^{\mathrm{rad}}$ distribution that resembles an inverted Gaussian along the $y$ axis. The $y$-component of the radiation force field in the chamber $\mathbf{F}_y^{\mathrm{rad}}$, derived from $U^{\mathrm{rad}}$ using Eq. (15), is responsible for focusing the particles at the center of the chamber by

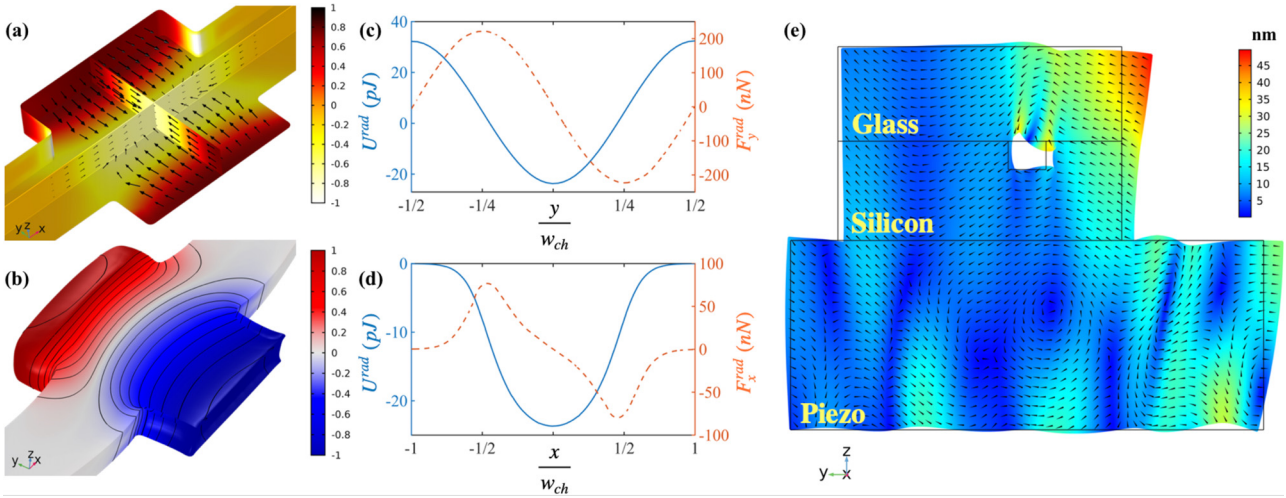


FIG. 2. (Color online) Numerical results for resonant frequency $f_r = 0.95$ MHz actuation in a silicon-glass device with asymmetry factor $\alpha = 0.5$ and transducer shift $l_s = 0$ mm. The device is filled with water and 20 $\mu$m silica microspheres and an electric potential of $V_p = 25$ (V) is applied to the transducer. (a) Normalized radiation force potential $U^{\mathrm{rad}}/U^{\mathrm{rad}}_{\mathrm{norm}}$ with $U^{\mathrm{rad}}_{\mathrm{norm}} = 57.7$ pJ and logarithmic arrow plot of $F^{\mathrm{rad}}$. (b) Color and contour plots of the normalized acoustic pressure field $P/P_{\mathrm{norm}}$ with $P_{\mathrm{norm}} = 8.5$ MPa and 3D deformation of the cavity walls around the chamber, the displacement field **u** is scaled by a factor of 2500 to be observable. [(c),(d)] Numerically calculated acoustic radiation potential and force field in $y$-$z$ and $x$-$z$ slices through the center of the chamber, respectively. (e) Color and vector plots of the displacement field **u** in an $x$-$y$ cut plane passing through the center of the chamber, depicting the deformation of the solid parts. The whole device is stretched in $z$ by a factor of 4 to get a clearer view of the chamber walls, and the deformation of the solid domain is scaled by a factor of 3000 for visibility purposes.

inducing migration in a direction perpendicular to the natural flow stream in the channel, thus, we will call this component the *focusing force*. Meanwhile, a similar distribution of $U^{\text{rad}}$ emerges along the $x$ axis and the resulting force component $\mathbf{F}_x^{\text{rad}}$ [Fig. 2(d)] is the reason why particles are forced to stay in the chamber, therefore, it is called the *trapping force*. The simultaneous presence of the focusing and trapping forces results in the aggregation of particles at the center of the chamber.

A strong focusing and trapping force field is required to collect the particles in the chamber effectively, therefore, driving the device at a resonance frequency is necessary to create a substantial acoustophoretic force field. The standing half wave resonance is expected to happen at $f_0$. However, the complex interplay between the various solids, the fluid– structure interaction at the cavity walls, and the nonuniform geometry of the microchannel leads us to sweep the frequencies from 0.5 to 2.15 MHz with more than 300 probes to study the frequency response from our 3D simulations. Previous methods have been proposed to quantitatively describe acoustic traps by calculating the stiffness (in $x$- and $y$-directions; Barmatz and Collas, 1985; Silva *et al.*, 2019). To identify actuation frequencies for aggregating particles in the center of the chamber, we use the ideal distribution of the radiation force potential, derived from a perfect half wave resonance, to establish a correlative relationship between the simulation results and the best-case scenario. The ideal radiation potential along $s = x$ or $y$ is defined as (Bruus, 2012c)

$$U_i^{\text{rad}}(s) = \left[\frac{f_1}{3}\cos^2(k_s s) - \frac{f_2}{2}\sin^2(k_s s)\right] \times \pi a^3 \kappa_{\text{fl}} P_0^2. \tag{21}$$

In order to generate a correlation coefficient between two arbitrary functions $f(s)$ and $g(s)$, we normalize the functions such that

$$\int_{-1}^{1} f(s)\,\mathrm{d}s = \int_{-1}^{1} g(s)\,\mathrm{d}s = 0, \tag{22a}$$

$$\int_{-1}^{1} f^2(s)\,\mathrm{d}s = \int_{-1}^{1} g^2(s)\,\mathrm{d}s = 1, \tag{22b}$$

and introduce the correlation coefficient as

$$r_s = \int_{-1}^{1} f(s)\,g(s)\mathrm{d}s. \tag{23}$$

The correlation coefficient factors $r_x$ and $r_y$, calculated using $f(s) = U_s^{\text{rad}}$ from simulations and $g(s) = U_i^{\text{rad}}$ of Eq. (21), show the quality of trapping and focusing acoustophoresis. Furthermore, to measure the intensity of the force field, we use the magnitude of the radiation potential inside the chamber, defined by

$$\Delta U_s^{\text{rad}} = \text{Max}\left(U_s^{\text{rad}}\right) - \text{Min}\left(U_s^{\text{rad}}\right). \tag{24}$$

Now we can set up a two-step process through which we can analyze the frequency response of our device with regard to the effectiveness and intensity of particle focusing and trapping in the center of the fluid-filled chamber. The first step is to calculate correlation coefficients and identify frequencies that result in combined focusing and trapping with relatively high quality. The second step is to measure force potential magnitudes at these frequencies to find resonances where focusing and trapping forces are maximized.

### B. Effects of device asymmetry on particle trapping acoustophoresis

Here, we use the said process to characterize six devices with identical micro-cavity designs but different chip asymmetry and piezo placement. In devices D1–D4, the transducer is simply actuated by a single electrode on the top surface of the piezo. In contrast, in devices D1a and D4a, the chip–transducer interface is spatially split and actuated in antiphase to better generate the conventional antisymmetric standing pressure half wave across the chamber (Moiseyenko and Bruus, 2019).

We begin by analysis of a symmetric transversal resonator (Lenshof *et al.*, 2012) device D1 with asymmetry factor $\alpha = 1$ and piezo shift $l_s = 0$ mm. The results of device characterization in Fig. 3(D1a) show the average acoustic energy densities in fluid and solid domains, and these values show fluid and solid resonances. However, high energies do not necessarily mean good acoustophoresis resulting in particle aggregation. Although resonant acoustic fields are a necessary condition for creating a strong force field, they do not serve as a sufficient condition because we need the energy to be higher in the chamber to result in local manipulation. Also, the force field must be oriented such that trapping and focusing forces are present at the same time.

To visualize results from the first step of our device characterization process, frequencies where $r_x$ and $r_y$ are greater than a threshold value $r_t = 0.9$ are highlighted by a series of yellow and blue bars, respectively. Green bands are generated when yellow and blue bars coalesce, meaning that the requirement for combined trapping and focusing is satisfied. Figure 3(D1b) summarizes the ability of the symmetric device to gather particles at the center of the chamber while showing the takeaway from the second step of the characterization process. We choose three peaks for comparison of device performance in different green bands within the frequency range. Peak number 1 is the only resonance around $\bar{f} = f/f_0 = 1$, where we expect to see a half wave, and it shows weaker force fields compared to peaks 2 and 3.

Analyzing device D2, where the silicon-glass chip has an asymmetry factor $\alpha = 1$ (symmetric chip) and the transducer is placed asymmetrically with $l_s = 2$ mm. Figure 3(D2a) shows that the maximum acoustic energy density in the whole device has increased compared to the previous case, and a much wider green band has formed around $\bar{f} = 1$; this event has been shown previously for devices with a straight channel (Garofalo *et al.*, 2017). We observe the highest values of the acoustic energy density are in the fluid domain around $\bar{f} = 2$, and they do not provide the desirable particle trapping as higher modes are in resonance

https://doi.org/10.1121/10.0001634

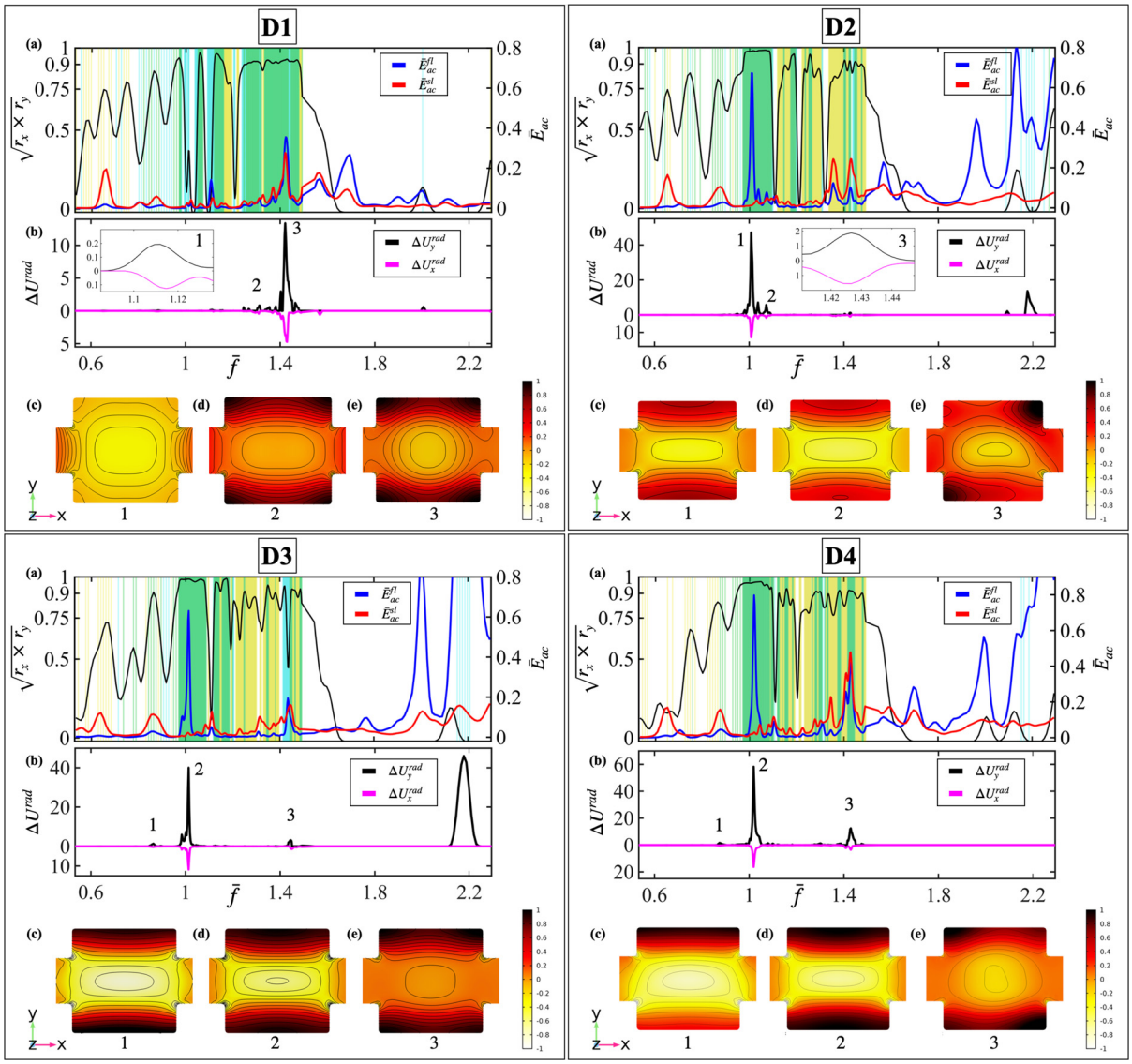


FIG. 3. (Color online) Plots of relevant acoustophoretic time-averaged fields versus normalized frequency $\bar{f} = f/f_0$ for frequencies between 0.5 and 2.15 MHz in devices D1–D4. (a) Blue and red lines show average acoustic energy density in fluid and solid domains, respectively. The solid black line shows combined focusing and trapping correlation coefficient values. Green regions show frequencies with well oriented forces for aggregating particles in the middle of the chamber. (b) The magnitude of the acoustic radiation potential field is shown for focusing (black) and trapping (magenta) with well oriented forces. [(c)–(e)] In each device, three peaks are chosen to be presented with further detail.

in those frequencies. It is also noteworthy that a significant amount of energy is stored in the cavity at the resonance around $\bar{f} = 1$, whereas the solid parts are not in resonance.

In Fig. 3(D2b), we see multiple strong peaks at approximately $\bar{f} = 1$ with desired trapping and focusing behaviors inside the chamber where the strongest peak has roughly 300 times more focusing radiation potential compared to its counterpart in D1 while the trapping potential is increased by a factor of 100. However, this device has a much weaker trapping potential at frequencies around $\bar{f} = 1.4$ in comparison to the previous case.

Next, we study D3 where the asymmetric chip with $\alpha = 0.5$ is placed on a piezo shifted by $l_s = 2$ mm. Figure 3(D3a) shows that the acoustic energy density resonances across the frequency range do not change significantly in comparison to D2. However, a noticeable difference between this case and the previous case would be that particle manipulation forces around $\bar{f} = 1.4$ are stronger for peak 3 in this device compared to the same resonance in D2. It is interesting that the resonance around $\bar{f} = 1$ remains relatively as strong as the one in D2 while a weak peak forms at $\bar{f} = 0.875$. As mentioned earlier, in peak 2, the acoustic energy resonance in the fluid domain is much stronger than in the solid parts, whereas the opposite can be said for peak 1. Therefore, we can use the concept of solid and fluid resonances (Moiseyenko and Bruus, 2019) to characterize peaks 1 and 2, respectively.

Last, we show results from the characterization of device D4 that consists of an asymmetric chip with $\alpha = 0.5$ and a piezo transducer that is placed symmetrically with

respect to the chamber, therefore, $l_s = 0$ mm. We can clearly see from Fig. 3 that D3 and D4 are very similar when it comes to the acoustophoresis quality, yet, the latter achieves force fields stronger by 50% at frequencies around $\bar{f} = 1$. It should be noted that the green band around $\bar{f} = 1.4$ is wider than in D2 and D3, and peak 3 shows much stronger focusing and trapping potential in comparison to the two previous cases. Energy densities are in resonance for both solid and fluid parts at this frequency.

In summary, under simple actuation, all asymmetric devices (D2, D3, D4) have their strongest acoustophoretic resonance very close to the predicted frequency for the standing half wave to form, while this resonance is the weakest in the symmetric device D1. Asymmetric chips excite noticeable fluid resonances as well as whole system resonances; however, symmetric chips produce fluid resonances only when the transducer is placed asymmetrically.

In the case of antisymmetric actuation of devices D1a and D4a, the standing pressure half wave resonance is promoted conceivably in our acoustofluidic chamber. Figure 4 shows that strong fluid and whole system resonances around $\bar{f} = 1$ are attainable in D1a. This device has the same layout as D1 except that the transducer is excited in antiphase. Acoustic focusing and trapping forces are, much like in D4, increased by more than 2 orders of magnitude compared to the symmetric case. It is noteworthy that the harmonic

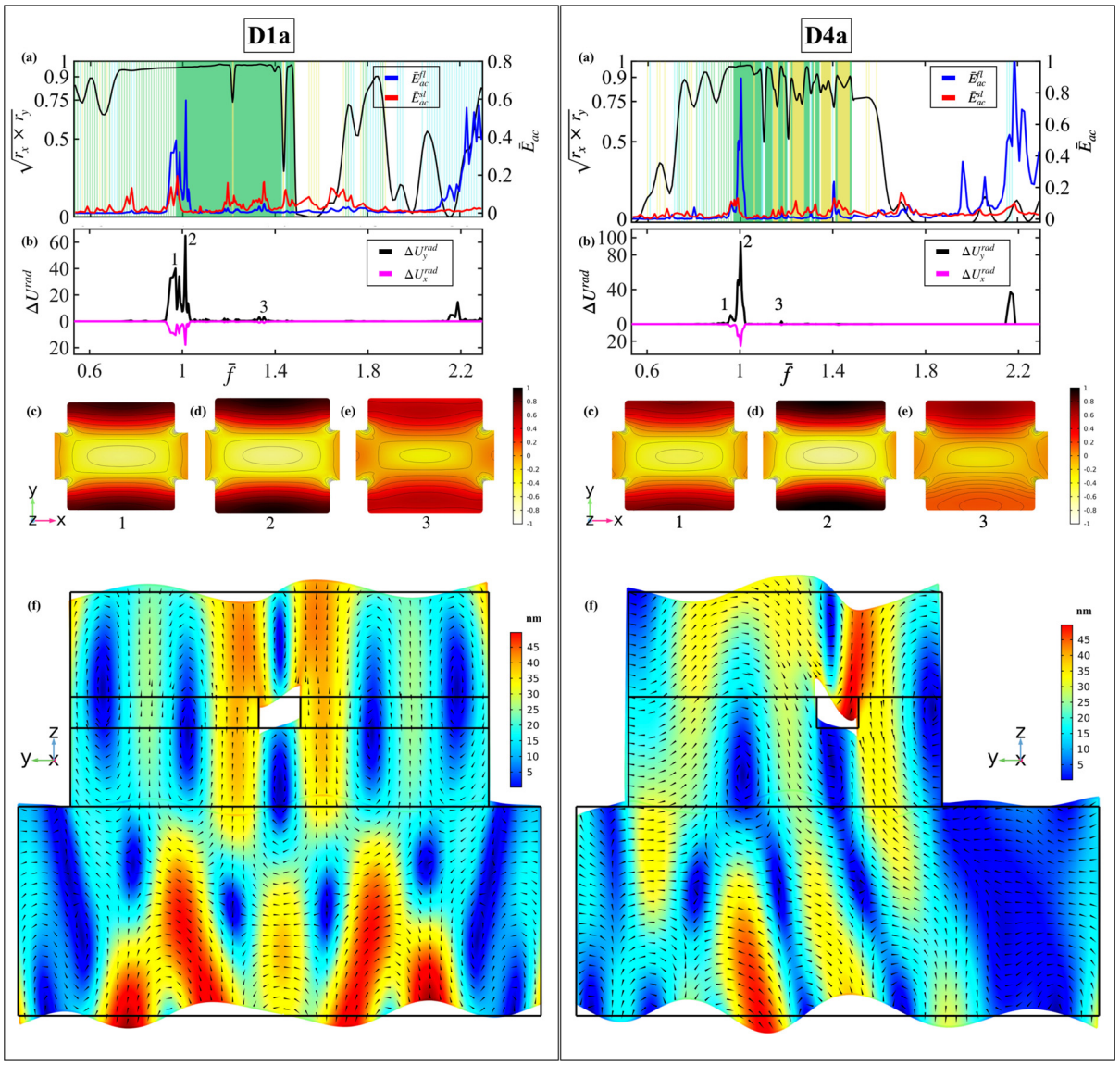


FIG. 4. (Color online) Plots of relevant acoustophoretic time-averaged fields versus normalized frequency $\bar{f} = f/f_0$ for frequencies between 0.5 and 2.15 MHz in devices D1a and D4a. (a) The average acoustic energy densities in fluid and solid domains are shown by blue and red lines, respectively. The solid black line shows combined focusing and trapping correlation coefficient values. Green bands signify frequencies with well oriented forces to trap particles in the center of the chamber. (b) The magnitude of the acoustic radiation force potential field is shown for focusing (black) and trapping (magenta) with well oriented forces. [(c)–(e)] In each device, three peaks are chosen to be presented with further detail. Normalized radiation potential fields represent the quality of acoustophoresis in the chamber, and the magnitudes of these fields are listed in Table IV. (f) Color and vector plots of the displacement field **u** in an $x$-$y$ cut plane passing through the center of the chamber, showing the deforming solids. The whole device is stretched in $z$ by a factor of 4 to get a clearer view of the chamber walls, and the deformation of the solid domain is scaled by a factor of 3000 for visibility purposes.

https://doi.org/10.1121/10.0001634

motion of the walls of the chamber are dominated by the top and bottom surfaces, which has led to a wide green band in D1a.

The strongest fluid resonance and trapping force fields are observed around $\bar{f} = 1$ when the asymmetric chip is actuated by an antisymmetric transducer as in D4a. In this device, the fluid–solid interaction resembles the one shown for D4 in Fig. 2(e). By comparison to the first four devices, in antisymmetrically actuated devices, the acoustophoretic resonance around $\bar{f} = 1.4$ is not excited at all. Normalized radiation potential fields represent the focusing and trapping acoustophoresis inside the chamber while the magnitudes of these fields are listed in Table IV.

### C. Experimental results

In the following, we process experimental data from video recordings to extract the transverse path of particles $y(t)$. We use image processing techniques (see SuppPub1.pdf, Sec. C in the supplementary material[1]) to track the vertical distances of particles from the center of our fluidic chamber while they migrate toward the pressure node. Devices used for experiments are analogous to the ones we simulated earlier, and the experiment is repeated ten times on each device to create a reliable data set supporting repeatability of the tests. In the experiments, particles start from the positions highlighted in Fig. 5(a) by light yellow, which correspond to trapping regions at $\bar{f} = 2$. This force field is generally stronger than the single node field we are investigating in this work, and it consistently holds particles in their initial positions across all devices. Immediately after switching to the predetermined resonant frequency around $f_0$, particles migrate to the center due to the acoustic radiation field shown in Fig. 5(b). The average distance travelled by particles under this scenario is roughly equal to $\lambda/8$ or a quarter of the chamber's width.

The average vertical location of particles $\bar{y}(t)$ is used to calculate the nondimensional transverse path, $\hat{y}(t)$ defined as

$$\hat{y}(t) = \frac{\bar{y}(t) - \bar{y}(t_\infty)}{\bar{y}(t_0) - \bar{y}(t_\infty)}, \tag{25}$$

which helps us compare particle aggregation times in devices D1–D4 more reliably by eliminating the effect of the aggregate thickness on the final position of the particles. The mean transverse path of the particles is presented in Fig. 5(c) for our array of devices, and it is clear that there is a difference between how particles are being manipulated in asymmetric devices versus in the symmetric devices. In order to test this hypothesis, we use an unequal variances $t$-test also known as Welch's test (Welch, 1951, 1947), which is suitable for showing independence of datasets in our case (Derrick and White, 2016; Ruxton, 2006). The $t_s$ statistic, showing whether the population means are different, is calculated as

$$t_s = \frac{\bar{y}_i - \bar{y}_j}{\sqrt{\frac{s_i^2}{N_i} + \frac{s_j^2}{N_j}}}, \tag{26}$$

where $\bar{y}_i$, $s_i^2$, and $N_i$ are the mean, variance, and size, respectively, of the $i$th sample. Evidently, the $t$-test shows that the means are similar at times before the migration starts because the microspheres are held at roughly the same distances from the center in all devices. Figures 5(d) and 5(g) show an example of the initial particle placement in devices D1 and D4, respectively. In Figs. 5(d)–5(i) raw images have

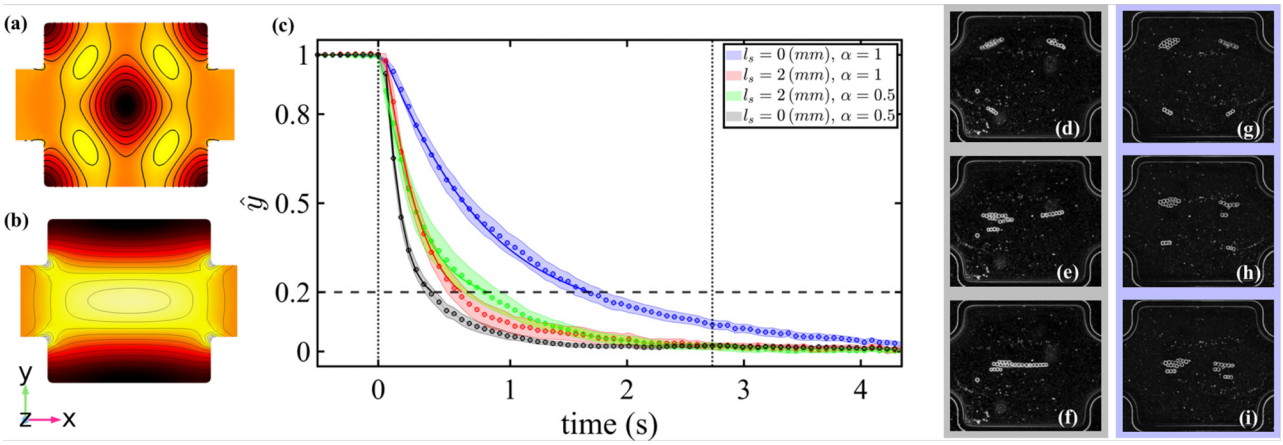


FIG. 5. (Color online) (a) Simulated acoustophoretic potential field for trapping particles in their initial position, at roughly $w_{ch}/4 = 200$ $\mu$m away from the center. (b) Simulated acoustophoretic potential field leading particles to their final positions in the middle of the chamber. (c) Summary of the experimental results showing nondimensional mean particle paths $\hat{y}(t)$ (circles), bounded by the standard error of the mean. Solid lines show the fitted curves given by Eq. (19), in which the transverse wavelength and the acoustic energy density are the fitting parameters. Colors blue, red, green, and black correspond to devices D1, D2, D3, and D4, respectively. Vertical dashed lines surround the portion of experimental data where the two-sample $t$-tests show significant differences [Eq. (26)] between the means of independent groups of experiments. The horizontal dashed line marks the vertical distance where interference from the secondary radiation force is considerable compared to the primary acoustic radiation force. [(d)–(f)] Video frames from an experiment on D4 showing positions of particles at $t = 0$ s, the beginning (d), followed by $t = 0.5$ s, marking an intermediate time (e) and final position of particles when $t = 2$ s (f). [(g)–(i)] Frames from an experiment on D1 at times equal to those of (d)–(f).

TABLE IV. Normalized frequency $\bar{f}$ and magnitude of acoustic radiation potential fields to focus ($\Delta U_y^{\text{rad}}$) and trap ($\Delta U_x^{\text{rad}}$) microparticles. These values are presented for three marked resonances in devices D1–D4, D1a, and D4a as shown in Figs. 3 and 4.

| Device | Peak | $\bar{f}$ | $\Delta U_y^{\text{rad}}$ (pJ) | $\Delta U_x^{\text{rad}}$ (pJ) |
|---|---|---|---|---|
| D1 | 1 | 1.1173 | 0.15 | 0.12 |
| | 2 | 1.312 | 0.85 | 0.42 |
| | 3 | 1.4213 | 13.38 | 4.67 |
| D2 | 1 | 1.008 | 47 | 12.8 |
| | 2 | 1.072 | 5.73 | 1.62 |
| | 3 | 1.4267 | 1.88 | 1.55 |
| D3 | 1 | 0.875 | 1.36 | 0.33 |
| | 2 | 1.0187 | 40 | 11.71 |
| | 3 | 1.448 | 2.65 | 1.32 |
| D4 | 1 | 0.864 | 1.63 | 0.43 |
| | 2 | 1.0133 | 57.7 | 16.28 |
| | 3 | 1.4293 | 12.45 | 3.56 |
| D1a | 1 | 0.9707 | 43.1 | 12.9 |
| | 2 | 1.0133 | 65.8 | 19.5 |
| | 3 | 1.352 | 3.8 | 1.3 |
| D4a | 1 | 0.96 | 13.7 | 5.8 |
| | 2 | 1.0027 | 94.8 | 27.2 |
| | 3 | 1.1787 | 4.3 | 1.6 |

been sharpened and edges are highlighted using ImageJ (Schneider *et al.*, 2012) software for clarity and visibility only.

After the piezo is set to the focusing resonance frequency, we can make a distinction with 99% confidence between the average transverse paths of particles in symmetric and asymmetric device data sets. The start of this event is marked by the dotted line on the left in Fig. 5(c) and qualitatively shown in Figs. 5(e) and 5(h). It should be noted that all devices create particle aggregates; therefore, after a period of time, the mean particle locations become similar enough that we cannot draw a confident distinction between data sets once more; the dotted line on the right in Fig. 5(c) shows this limit.

In the following, we use the curve fitting routine of Sec. III B) with acoustic energy density $E_{\text{ac}}$ and wavenumber $k_y$ as the fitting parameters for Eq. (19). The nonlinear least squares method in MATLAB (The MathWorks, Natick, MA) is used to fit this function to experimental data points, and we get a relatively good fit in the region where particles are mainly driven by primary acoustic radiation force and Stokes' drag. Extracted fit parameters are listed in Table V along with the resonant actuation frequencies in experiments and predicted resonances from simulations. The estimated values of the chamber width obtained by the fit closely represent the actual value, and the disparity may be due to inter-particle forces and the pressure node in the experiments does not necessarily form exactly in the center of the chamber. The relationship between energies in different devices shows a good qualitative agreement with simulation results where D4 has the strongest force field and D1 shows a weak resonance at frequencies around 1 MHz Therefore, we expect to see particle aggregates forming faster in an asymmetric device compared to a symmetric device. This is shown in Figs. 5(f) and 5(i) where after the same amount of time, particles in D4 have already formed a tight group while in D1, they have not assumed their final position yet. More information about the image processing techniques, *t*-tests, and curve fitting is available in the supplementary material (see SuppPub1.pdf, Sec. B).[1]

TABLE V. Fitted parameters $E_{\text{ac}}$ and $w_{\text{ch}}$ to experimental data. Predicted nondimensional resonance frequency from simulations $\bar{f}_{\text{sim}}$ and frequency range for all experimental resonances $\bar{f}_{\text{exp}}$ used in each device.

| Device | $E_{\text{ac}}$ (J/m$^3$) | $w_{\text{ch}}$ ($\mu$m) | $\bar{f}_{\text{exp}}$ | $\bar{f}_{\text{sim}}$ |
|---|---|---|---|---|
| D1 | 0.71 | 750 | 1.04–1.14 | 1.12 |
| D2 | 2.22 | 742 | 1.02–1.04 | 1.01 |
| D3 | 2.38 | 796 | 1.03–1.04 | 1.02 |
| D4 | 5.09 | 756 | 1.02–1.03 | 1.01 |

## V. DISCUSSION

In this study, we use COMSOL Multiphysics 5.4a to simulate microparticle acoustophoresis by acoustic radiation in BAW devices. The 3D numerical model that is developed based on well-defined previous theoretical work (Bach and Bruus, 2018; Bruus, 2012a; Hahn and Dual, 2015; Ley and Bruus, 2017) includes the piezoelectric transducer, the silicon chip, the glass reflector layer, and the water-filled cavity. Such simulations are used to characterize device performance and design micro-acousto-fluidic systems for strong and effective acoustophoresis. We use frequency-dependent time-averaged acoustophoretic fields to analyze the strength and quality of acoustophoresis with regard to a desired force field. By using this method, the process of finding resonances will be streamlined in an experimental setup and the device design and testing process will become more efficient.

The 3D features of the device we study and the importance of determining the mode shapes of acoustic fields obligate developing a 3D simulation for analyzing the performance of such acoustic traps. Our model can predict resonant frequencies for strong trapping acoustophoresis that are in good agreement with experimental results.

In BAW devices with rigid walls, the solid components run the fluid for the most part, and the scattered pressure waves are predominantly dependent on the movement of cavity walls. We find that the antisymmetric translational displacement of solid walls is required for setting up an ultrasonic standing half wave across the chamber (Bora and Shusteff, 2015; Reichert *et al.*, 2018). However, the vertical actuation mode of the piezo used in this work does not excite the desired transverse motion (Garofalo *et al.*, 2017). We show that acoustophoresis for particle aggregation can be improved by either shifting piezo placement or designing the chip asymmetrically when the transducer is actuated by a single electrode. The asymmetric chip provides improved acoustophoresis regardless of the piezo placement as the asymmetry becomes a characteristic of the coupled

https://doi.org/10.1121/10.0001634

fluid–solid domain. By comparing the acoustophoresis results from devices D4, D1a, and D4a, we have shown that asymmetric chip design can improve the device performance as much as the method of "antisymmetric piezo actuation" proposed in Moiseyenko and Bruus (2019).

Looking at the results of Figs. 4, 5, and Table IV, we can see that a symmetric chip and piezo arrangement (D1) is suited to trap particles by producing an even (1–1) mode around $\bar{f} = \sqrt{2}$. Additionally, this chip design produces strong half wave resonances if actuation on the split electrode is changed from in-phase to antiphase (D1a). While the combination of an asymmetric chip and antisymmetric transducer (D4a) produces the strongest half wave resonance, device D4 can excite the even mode and the half wave resonances to relatively high amplitudes. In-phase actuation of the asymmetric chip results in the ability to excite various strong acoustophoretic resonances in the same device (D4). This feature has various advantages from an applications point of view.

Acoustic energy densities in fluid and solid parts are a useful indicator of resonant frequencies and the domain in resonance. Although the solids make up a much larger portion of the device, the fluid can hold an incredible amount of energy when in resonance, and our observations show that these decoupled resonances deliver stronger acoustophoresis and are only available in asymmetric devices. On the other hand, strong acoustophoresis in a symmetric device is only observed when fluid and solids are in simultaneous resonance.

Comparing energy densities of devices at resonance does not truly reflect the difference in strength of the acoustophoretic field in the chamber even if the correlation factors guarantee high-quality manipulation. This is demonstrated by looking at peak 1 in devices D1 and D2, where acoustic energies are higher by a factor of 4 in the latter and radiation forces are larger by 2 orders of magnitude. An explanation for this disparity is that energy may be high in the areas outside the chamber, creating strong acoustophoresis in the channel; also energy dense regions around the corners increase the total density while they do not contribute to particle manipulation in the main part of the cavity. To avoid these errors, the trapping and focusing fields within the target manipulation region must be used to reasonably compare device performances.

Experimental results show a statistically significant reduction in the particle aggregation time as a result of using an asymmetric device design [see experimental videos SuppPubmm4.mp4 (D1, 1.072 MHz-15 fps) and SuppPubmm5.mp4 (D4, 0.955 MHz-15 fps) in the supplementary material].[1] We established a trend showing an improvement of particle manipulation with breaking device symmetry in simulations, and a similar development is observed in an array of experiments in spite of the fact that the model neglects some damping sources and effects, such as particle–particle interactions and streaming, induced drag.

It is noteworthy that while symmetric devices with compression/extension mode of actuation are not optimal for setting up half wave resonances, they are quite suitable for creating the so-called (1–1) resonant mode (Leibacher *et al.*, 2014a) at frequencies around $\bar{f} = \sqrt{2}$ when a standing pressure wave forms along the diagonals of the square chamber. This can be explained by relating the required displacement of the cavity walls and the main deformation mode of the transducer. Vertical motion of the top and bottom walls gives rise to this pressure distribution and intuitively aligning the center of the device with the center of the piezo results in high amplitude pressure fields. The effect of aligning the piezo with the chamber can also be seen in D4 where symmetric placement of an asymmetric device has strengthened the (1–1) resonance. In devices D1a and D4a, this resonance vanishes and the half wave mode becomes dominant in a large range of frequencies because the antisymmetric actuation of the transducer dictates an asymmetric motion of the channel walls.

This work focuses on a device produced for particle trapping; however, the simulations and device characterization methods can be tailored to any BAW device with a well-defined target force field as long as the theoretical framework is applicable to the materials used for fabrication and relative length scales of the acoustic fields, the device, and particles.

## VI. CONCLUSION

We investigate the effects of asymmetric device design on improving acoustophoresis in a microfluidic chamber. Simulation results demonstrate that geometrical asymmetry of the device can result in substantially stronger particle trapping fields through exciting naturally antisymmetric solid displacement modes in frequencies around $\bar{f} = 1$, where the goal is to excite a standing half wave. A series of experiments are conducted to inspect simulated results. Image processing analyses of experimental observations reveal a meaningful improvement in the particle aggregation time by using asymmetric devices. We present these experimental results as a proof of concept.

Based on the examples presented in this paper, we believe that asymmetric chip structure has the potential of being used as a general design element. The increased acoustic force fields in the devices have a major impact on manipulating particles with a low acoustic contrast factor (Augustsson *et al.*, 2010), high throughput 3D printing (Friedrich *et al.*, 2017), lab-on-a-chip applications (Ohlin *et al.*, 2015), and potential chemical detection in microfluidic devices (Piorek *et al.*, 2007). It would be interesting to develop complete models of asymmetric devices with acoustic streaming and take into account the thermoviscous effects (Muller and Bruus, 2014) to capture acoustophoretic behavior of particles smaller than the critical size (Muller *et al.*, 2012). This information can be used to create reliable time dependent simulations (Baasch *et al.*, 2017; Hahn *et al.*, 2015) of particle motion and obtain valuable information about particle assembly patterns.

## ACKNOWLEDGMENTS

We thank Dr. Tyler Ray for his helpful comments and Mr. Nicholas Judy who assisted with microfabrication.

Fabrication was done at the University of California, Santa Barbara, Nanofabrication Facility, which is part of the National Science Foundation–funded National Nanofabrication Infrastructure Network. This work was supported by the Institute for Collaborative Biotechnologies through Contract No. W911NF-09-D-0001.

[1]See supplementary material at https://doi.org/10.1121/10.0001634 for multimedia files (animations and videos) and a detailed explanation of the grid convergence study, statistical analysis, and image processing.


Adams, J. D., Ebbesen, C. L., Barnkob, R., Yang, A. H. J., Soh, H. T., and Bruus, H. (**2012**). "High-throughput, temperature-controlled microchannel acoustophoresis device made with rapid prototyping," J. Micromech. Microeng. **22**, 075017.

Antfolk, M., and Laurell, T. (**2017**). "Continuous flow microfluidic separation and processing of rare cells and bioparticles found in blood—A review," Anal. Chim. Acta **965**, 9–35.

Antfolk, M., Muller, P. B., Augustsson, P., Bruus, H., and Laurell, T. (**2014**). "Focusing of sub-micrometer particles and bacteria enabled by two-dimensional acoustophoresis," Lab Chip **14**, 2791–2799.

Augustsson, P., Barnkob, R., Grenvall, C., Deierborg, T., Brundin, P., Bruus, H., and Laurell, T. (**2010**). "Measuring the acoustophoretic contrast factor of living cells in microchannels," in *Proc. 14th Int. Conf. Miniaturized Syst. Chem. Life Sci.*, Groningen, The Netherlands, pp. 1337–1339.

Augustsson, P., Barnkob, R., Wereley, S. T., Bruus, H., and Laurell, T. (**2011**). "Automated and temperature-controlled micro-PIV measurements enabling long-term-stable microchannel acoustophoresis characterization," Lab Chip **11**, 4152–4164.

Augustsson, P., Magnusson, C., Nordin, M., Lilja, H., and Laurell, T. (**2012**). "Microfluidic, label-free enrichment of prostate cancer cells in blood based on acoustophoresis," Anal. Chem. **84**, 7954–7962.

Augustsson, P., Persson, J., Ekström, S., Ohlin, M., and Laurell, T. (**2009**). "Decomplexing biofluids using microchip based acoustophoresis," Lab Chip **9**, 810–818.

Baasch, T., Leibacher, I., and Dual, J. (**2017**). "Multibody dynamics in acoustophoresis," J. Acoust. Soc. Am. **141**, 1664–1674.

Bach, J. S., and Bruus, H. (**2018**). "Theory of pressure acoustics with viscous boundary layers and streaming in curved elastic cavities," J. Acoust. Soc. Am. **144**, 766–784.

Baresch, D., Thomas, J.-L., and Marchiano, R. (**2016**). "Observation of a single-beam gradient force acoustical trap for elastic particles: Acoustical tweezers," Phys. Rev. Lett. **116**, 024301.

Barmatz, M., and Collas, P. (**1985**). "Acoustic radiation potential on a sphere in plane, cylindrical, and spherical standing wave fields," J. Acoust. Soc. Am. **77**, 928–945.

Barnkob, R., Augustsson, P., Laurell, T., and Bruus, H. (**2010**). "Measuring the local pressure amplitude in microchannel acoustophoresis," Lab Chip **10**, 563–570.

Barnkob, R., Augustsson, P., Laurell, T., and Bruus, H. (**2012**). "Acoustic radiation- and streaming-induced microparticle velocities determined by microparticle image velocimetry in an ultrasound symmetry plane," Phys. Rev. E **86**, 056307.

Begley, M. R., Gianola, D. S., and Ray, T. R. (**2019**). "Bridging functional nanocomposites to robust macroscale devices," Science **364**(6447), eaav4299.

Bjerknes, V. (**1906**). *Fields of Force: Supplementary Lectures, Applications to Meteorology; A Course of Lectures in Mathematical Physics delivered December 1 to 23, 1905*, 1st ed. (The Columbia University Press, New York).

Bora, M., and Shusteff, M. (**2015**). "Efficient coupling of acoustic modes in microfluidic channel devices," Lab Chip **15**, 3192–3202.

Bruus, H. (**2011**). "Acoustofluidics 1: Governing equations in microfluidics," Lab Chip **11**, 3742–3751.

Bruus, H. (**2012a**). "Acoustofluidics 2: Perturbation theory and ultrasound resonance modes," Lab Chip **12**, 20–28.

Bruus, H. (**2012b**). "Acoustofluidics 10: Scaling laws in acoustophoresis," Lab Chip **12**, 1578–1586.

Bruus, H. (**2012c**). "Acoustofluidics 7: The acoustic radiation force on small particles," Lab Chip **12**, 1014–1021.

Burguillos, M. A., Magnusson, C., Nordin, M., Lenshof, A., Augustsson, P., Hansson, M. J., Elmér, E., Lilja, H., Brundin, P., Laurell, T., and Deierborg, T. (**2013**). "Microchannel acoustophoresis does not impact survival or function of microglia, leukocytes or tumor cells," PLoS One **8**, e64233.

Collino, R. R., Ray, T. R., Fleming, R. C., Cornell, J. D., Compton, B. G., and Begley, M. R. (**2016**). "Deposition of ordered two-phase materials using microfluidic print nozzles with acoustic focusing," Extrem. Mech. Lett. **8**, 96–106.

Collino, R. R., Ray, T. R., Fleming, R. C., Sasaki, C. H., Haj-Hariri, H., and Begley, M. R. (**2015**). "Acoustic field controlled patterning and assembly of anisotropic particles," Extrem. Mech. Lett. **5**, 37–46.

Collino, R. R., Ray, T. R., Friedrich, L. M., Cornell, J. D., Meinhart, C. D., and Begley, M. R. (**2018**). "Scaling relationships for acoustic control of two-phase microstructures during direct-write printing," Mater. Res. Lett. **6**, 191–198.

Collins, D. J., Devendran, C., Ma, Z., Ng, J. W., Neild, A., and Ai, Y. (**2016**). "Acoustic tweezers via sub–time-of-flight regime surface acoustic waves," Sci. Adv. **2**, e1600089.

Collins, D. J., Morahan, B., Garcia-Bustos, J., Doerig, C., Plebanski, M., and Neild, A. (**2015**). "Two-dimensional single-cell patterning with one cell per well driven by surface acoustic waves," Nat. Commun. **6**, 8686.

Derrick, B., and White, P. (**2016**). "Why Welch's test is type I error robust," Quant. Methods Psychol. **12**, 30–38.

Doinikov, A. A. (**1999**). "Bjerknes forces between two bubbles in a viscous fluid," J. Acoust. Soc. Am. **106**, 3305–3312.

Doinikov, A. A., and Zavtrak, S. T. (**1995**). "On the mutual interaction of two gas bubbles in a sound field," Phys. Fluids **7**, 1923–1930.

Drinkwater, B. W. (**2016**). "Dynamic-field devices for the ultrasonic manipulation of microparticles," Lab Chip **16**, 2360–2375.

Dual, J., and Möller, D. (**2012**). "Acoustofluidics 4: Piezoelectricity and application in the excitation of acoustic fields for ultrasonic particle manipulation," Lab Chip **12**, 506–514.

Dual, J., and Schwarz, T. (**2012**). "Acoustofluidics 3: Continuum mechanics for ultrasonic particle manipulation," Lab Chip **12**, 244–252.

Evander, M., Gidlöf, O., Olde, B., Erlinge, D., and Laurell, T. (**2015**). "Non-contact acoustic capture of microparticles from small plasma volumes," Lab Chip **15**, 2588–2596.

Evander, M., Johansson, L., Lilliehorn, T., Piskur, J., Lindvall, M., Johansson, S., Almqvist, M., Laurell, T., and Nilsson, J. (**2007**). "Noninvasive acoustic cell trapping in a microfluidic perfusion system for online bioassays," Anal. Chem. **79**(7), 2984–2991.

Evander, M., Lenshof, A., Laurell, T., and Nilsson, J. (**2008**). "Acoustophoresis in wet-etched glass chips," Anal. Chem. **80**, 5178–5185.

Foresti, D., Kroll, K. T., Amissah, R., Sillani, F., Homan, K. A., Poulikakos, D., and Lewis, J. A. (**2018**). "Acoustophoretic printing," Sci. Adv. **4**, eaat1659.

Friedrich, L., Collino, R., Ray, T., and Begley, M. (**2017**). "Acoustic control of microstructures during direct ink writing of two-phase materials," Sens. Actuators, A **268**, 213–221.

Garofalo, F., Laurell, T., and Bruus, H. (**2017**). "Performance study of acoustophoretic microfluidic silicon-glass devices by characterization of material- and geometry-dependent frequency spectra," Phys. Rev. Appl. **7**, 054026.

Gautam, G. P., Burger, T., Wilcox, A., Cumbo, M. J., Graves, S. W., and Piyasena, M. E. (**2018**). "Simple and inexpensive micromachined aluminum microfluidic devices for acoustic focusing of particles and cells," Anal. Bioanal. Chem. **410**, 3385–3394.

González, I., Tijero, M., Martin, A., Acosta, V., Berganzo, J., Castillejo, A., Bouali, M., and Soto, J. L. (**2015**). "Optimizing polymer lab-on-chip platforms for ultrasonic manipulation: Influence of the substrate," Micromachines **6**, 574–591.

Gor'kov, L. P. (**1962**). "On the forces acting on a small particle in an acoustical field in an ideal fluid," Sov. Phys. Dokl. **6**, 773–775.

Grenvall, C., Folkenberg, J. R., Augustsson, P., and Laurell, T. (**2012**). "Label-free somatic cell cytometry in raw milk using acoustophoresis," Cytom. Part A **81A**, 1076–1083.

Guo, J., Kang, Y., and Ai, Y. (**2015**). "Radiation dominated acoustophoresis driven by surface acoustic waves," J. Colloid Interface Sci. **455**, 203–211.

Hagsäter, S. M., Jensen, T. G., Bruus, H., and Kutter, J. P. (**2007**). "Acoustic resonances in microfluidic chips: Full-image micro-PIV experiments and numerical simulations," Lab Chip **7**, 1336–1344.

Hahn, P., and Dual, J. (**2015**). "A numerically efficient damping model for acoustic resonances in microfluidic cavities," Phys. Fluids **27**, 062005.
Hahn, P., Leibacher, I., Baasch, T., and Dual, J. (**2015**). "Numerical simulation of acoustofluidic manipulation by radiation forces and acoustic streaming for complex particles," Lab Chip **15**, 4302–4313.
Hahn, P., Schwab, O., and Dual, J. (**2014**). "Modeling and optimization of acoustofluidic micro-devices," Lab Chip **14**, 3937–3948.
Hammarström, B., Evander, M., Barbeau, H., Bruzelius, M., Larsson, J., Laurell, T., and Nilsson, J. (**2010**). "Non-contact acoustic cell trapping in disposable glass capillaries," Lab Chip **10**, 2251–2257.
Hammarström, B., Evander, M., Wahlström, J., and Nilsson, J. (**2014**). "Frequency tracking in acoustic trapping for improved performance stability and system surveillance," Lab Chip **14**, 1005–1013.
Hammarström, B., Laurell, T., and Nilsson, J. (**2012**). "Seed particle-enabled acoustic trapping of bacteria and nanoparticles in continuous flow systems," Lab Chip **12**, 4296–4304.
Hopcroft, M. A., Hopcroft, M. A., Nix, W. D., and Kenny, T. W. (**2010**). "What is the Young's modulus of silicon," J. Microelectromech. Syst. **2010**, 229–238.
Iranmanesh, I., Barnkob, R., Bruus, H., and Wiklund, M. (**2013**). "Tunable-angle wedge transducer for improved acoustophoretic control in a microfluidic chip," J. Micromech. Microeng. **23**, 105002.
Karlsen, J. T., and Bruus, H. (**2015**). "Forces acting on a small particle in an acoustical field in a thermoviscous fluid," Phys. Rev. E **92**, 043010.
Karthick, S., and Sen, A. K. (**2018**). "Improved understanding of acoustophoresis and development of an acoustofluidic device for blood plasma separation," Phys. Rev. Appl. **10**, 034037.
Laurell, T., and Lenshof, A. (eds.) (**2014**). *Microscale Acoustofluidics* (Royal Society of Chemistry, Cambridge, UK).
Leibacher, I., Dietze, W., Hahn, P., Wang, J., Schmitt, S., and Dual, J. (**2014a**). "Acoustophoresis of hollow and core-shell particles in two-dimensional resonance modes," Microfluid. Nanofluid. **16**, 513–524.
Leibacher, I., Reichert, P., and Dual, J. (**2015**). "Microfluidic droplet handling by bulk acoustic wave (BAW) acoustophoresis," Lab Chip **15**, 2896–2905.
Leibacher, I., Schatzer, S., and Dual, J. (**2014b**). "Impedance matched channel walls in acoustofluidic systems," Lab Chip **14**, 463–470.
Lenshof, A., Evander, M., Laurell, T., and Nilsson, J. (**2012**). "Acoustofluidics 5: Building microfluidic acoustic resonators," Lab Chip **12**, 684–695.
Ley, M. W. H., and Bruus, H. (**2017**). "Three-dimensional numerical modeling of acoustic trapping in glass capillaries," Phys. Rev. Appl. **8**, 024020.
Lin, S.-C. S., Mao, X., and Huang, T. J. (**2012**). "Surface acoustic wave (SAW) acoustophoresis: Now and beyond," Lab Chip **12**, 2766–2770.
Lissandrello, C., Dubay, R., Kotz, K. T., and Fiering, J. (**2018**). "Purification of lymphocytes by acoustic separation in plastic microchannels," SLAS Technol. Transl. Life Sci. Innov. **23**, 352–363.
Lopes, J. H., Azarpeyvand, M., and Silva, G. T. (**2016**). "Acoustic interaction forces and torques acting on suspended spheres in an ideal fluid," IEEE Trans. Ultrason. Ferroelectr. Freq. Control **63**, 186–197.
Manneberg, O., Vanherberghen, B., Svennebring, J., Hertz, H. M., Önfelt, B., and Wiklund, M. (**2008**). "A three-dimensional ultrasonic cage for characterization of individual cells," Appl. Phys. Lett. **93**, 063901.
Melchert, D. S., Collino, R. R., Ray, T. R., Dolinski, N. D., Friedrich, L., Begley, M. R., and Gianola, D. S. (**2019**). "Flexible conductive composites with programmed electrical anisotropy using acoustophoresis," Adv. Mater. Technol. **4**(12), 1900586.
Moiseyenko, R. P., and Bruus, H. (**2019**). "Whole-system ultrasound resonances as the basis for acoustophoresis in all-polymer microfluidic devices," Phys. Rev. Appl. **11**, 014014.
Muller, P. B., Barnkob, R., Jensen, M. J. H., and Bruus, H. (**2012**). "A numerical study of microparticle acoustophoresis driven by acoustic radiation forces and streaming-induced drag forces," Lab Chip **12**, 4617–4627.
Muller, P. B., and Bruus, H. (**2014**). "Numerical study of thermoviscous effects in ultrasound-induced acoustic streaming in microchannels," Phys. Rev. E **90**, 043016.
Muller, P. B., and Bruus, H. (**2015**). "Theoretical study of time-dependent, ultrasound-induced acoustic streaming in microchannels," Phys. Rev. E **92**, 063018.
Muller, P. B., Rossi, M., Marín, Á. G., Barnkob, R., Augustsson, P., Laurell, T., Kähler, C. J., and Bruus, H. (**2013**). "Ultrasound-induced acoustophoretic motion of microparticles in three dimensions," Phys. Rev. E **88**, 023006.
Nama, N., Barnkob, R., Mao, Z., Kähler, C. J., Costanzo, F., and Huang, T. J. (**2015**). "Numerical study of acoustophoretic motion of particles in a PDMS microchannel driven by surface acoustic waves," Lab Chip **15**, 2700–2709.
Ohlin, M., Iranmanesh, I., Christakou, A. E., and Wiklund, M. (**2015**). "Temperature-controlled MPa-pressure ultrasonic cell manipulation in a microfluidic chip," Lab Chip **15**, 3341–3349.
Ohlsson, P., Evander, M., Petersson, K., Mellhammar, L., Lehmusvuori, A., Karhunen, U., Soikkeli, M., Seppa, T., Tuunainen, E., Spangar, A., von Lode, P., Rantakokko-Jalava, K., Otto, G., Scheding, S., Soukka, T., Wittfooth, S, and Laurell, T. (**2016**). "Integrated acoustic separation, enrichment, and microchip polymerase chain reaction detection of bacteria from blood for rapid sepsis diagnostics," Anal. Chem. **88**, 9403–9411.
Petersson, F., Åberg, L., Swärd-Nilsson, A. M., and Laurell, T. (**2007**). "Free flow acoustophoresis: Microfluidic-based mode of particle and cell separation," Anal. Chem. **79**, 5117–5123.
Piorek, B. D., Lee, S. J., Santiago, J. G., Moskovits, M., Banerjee, S., and Meinhart, C. D. (**2007**). "Free-surface microfluidic control of surface-enhanced Raman spectroscopy for the optimized detection of airborne molecules," Proc. Natl. Acad. Sci. U.S.A. **104**, 18898–18901.
Reichert, P., Deshmukh, D., Lebovitz, L., and Dual, J. (**2018**). "Thin film piezoelectrics for bulk acoustic wave (BAW) acoustophoresis," Lab Chip **18**, 3655–3667.
Ruxton, G. D. (**2006**). "The unequal variance *t*-test is an underused alternative to student's *t*-test and the Mann–Whitney U test," Behav. Ecol. **17**, 688–690.
Samarasekera, C., and Yeow, J. T. W. (**2015**). "Facile microfluidic channels for acoustophoresis on a budget," Biomed. Microdevices **17**, 99.
Schneider, C. A., Rasband, W. S., and Eliceiri, K. W. (**2012**). "NIH image to ImageJ: 25 years of image analysis," Nat. Methods **9**, 671–675.
Settnes, M., and Bruus, H. (**2012**). "Forces acting on a small particle in an acoustical field in a viscous fluid," Phys. Rev. E **85**, 016327.
Shi, J., Ahmed, D., Mao, X., Lin, S.-C. S., Lawit, A., and Huang, T. J. (**2009**). "Acoustic tweezers: Patterning cells and microparticles using standing surface acoustic waves (SSAW)," Lab Chip **9**, 2890–2895.
Silva, G. T., and Bruus, H. (**2014**). "Acoustic interaction forces between small particles in an ideal fluid," Phys. Rev. E **90**, 063007.
Silva, G. T., Lopes, J. H., Leão-Neto, J. P., Nichols, M. K., and Drinkwater, B. W. (**2019**). "Particle patterning by ultrasonic standing waves in a rectangular cavity," Phys. Rev. Appl. **10**, 54044.
Skov, N. R., Bach, J. S., Winckelmann, B. G., and Bruus, H. (**2019a**). "3D modeling of acoustofluidics in a liquid-filled cavity including streaming, viscous boundary layers, surrounding solids, and a piezoelectric transducer," AIMS Math. **4**, 99–111.
Skov, N. R., Sehgal, P., Kirby, B. J., and Bruus, H. (**2019b**). "Three-dimensional numerical modeling of surface-acoustic-wave devices: Acoustophoresis of micro- and nanoparticles including streaming," Phys. Rev. Appl. **12**, 044028.
Thévoz, P., Adams, J. D., Shea, H., Bruus, H., and Soh, H. T. (**2010**). "Acoustophoretic synchronization of mammalian cells in microchannels," Anal. Chem. **82**, 3094–3098.
Welch, B. L. (**1947**). "The generalization of 'student's' problem when several different population varlances are involved," Biometrika **34**, 28–35.
Welch, B. L. (**1951**). "On the comparison of several mean values: An alternative approach," Biometrika **38**, 330–336.
Yang, A. H. J., and Soh, H. T. (**2012**). "Acoustophoretic sorting of viable mammalian cells in a microfluidic device," Anal. Chem. **84**, 10756–10762.
Zalis, M. C., Reyes, J. F., Augustsson, P., Holmqvist, S., Roybon, L., Laurell, T., and Deierborg, T. (**2016**). "Label-free concentration of viable neurons, hESCs and cancer cells by means of acoustophoresis," Integr. Biol. **8**, 332–340.
Zmijan, R., Jonnalagadda, U. S., Carugo, D., Kochi, Y., Lemm, E., Packham, G., Hill, M., and Glynne-Jones, P. (**2015**). "High throughput imaging cytometer with acoustic focussing," RSC Adv. **5**, 83206–83216.